A modular spiral phase plate design for orbital angular momentum generation at millimetre wavelengths

Peter Schemmel,* Giampaolo Pisano, and Bruno Maffei

Jodrell Bank Centre for Astrophysics, School of Physics and Astronomy, University of Manchester, Oxford Road, Manchester M13 9PL, UK

*peter.schemmel@postgrad.manchester.ac.uk

Abstract: Proof of concept measurements of a modular spiral phase plate design able to generate millimetre wavelength beams with an azimuthal mode number of $l = \pm 10$ are presented. The plate is comprised of ten single modules that interlock to create the full plate assembly, allowing improved machining accuracy compared to standard techniques. Therefore, this design could be used in millimetre wavelength systems that require the manipulation of large OAM modes. The plate was manufactured from polypropylene (index of refraction $n \approx 1.5$), and was measured at 100 GHz. A three dimensional field scanner was used to measure three near field surfaces behind the plate. Intensity measurements showed the expected OAM intensity ring, and phase measurements showed ten phase dislocations, implying proper functionality.

OCIS codes: (120.5050) Phase measurements; (120.5060) Phase modulation; (120.5800) Scanners; (350.5500) Propagation; (350.5030) Phase; (350.4010) Microwaves.

References and links

1. J. Wang, J. Yang, I.M. Frazal, N. Ahmed, Y. Yan, H. Huang, Y. Ren, Y. Yue, S. Dolinar, M. Tur, and A.E. Willner, "Terabit free-space data transmission employing orbital angular momentum multiplexing," Nature Photon. **6**, 488-496 (2012).
2. H. Huang, G. Xie, Y. Yan, N. Ahmed, Y. Ren, Y. Yue, D. Rogawski, M. J. Willner, B. I. Erkmen, K. M. Birnbaum, S. J. Dolinar, M. P. J. Lavery, M. J. Padgett, M. Tur and A. E. Willner, "100 Tbit/s free-space data link enabled by three-dimensional multiplexing of orbital angular momentum, polarization and wavelength," Opt. Lett. **39**, 197-200 (2014).
3. I. M. Frazal, N. Ahmed, J. Wang, J. Y. Yang, Y. Yan, B. Shamee, H. Huang, Y. Yue, S. Dolinar, M. Tur, and A. E. Willner, "2 Tbit/s free-space data transmission on two orthogonal orbital-angular-momentum beams each carrying 25 WDM channels," Opt. Lett. **37**, 4753-4755 (2012).
4. F. Tamburini, E. Mari, A. Sponselli, B. Thidé, A. Bianchini, and F. Romanato, "Encoding many channels on the same frequency through radio vorticity: first experimental test," New J. Phys. **14**, 033001 (2012).
5. D. J. Sanchez, D. W. Oesch and O. R. Reynolds, "The creation of photonic orbital angular momentum in electromagnetic waves propagating through turbulence," A&A **556**, A130 (2013).
6. M. Harwit, "Photon Orbital Angular Momentum in Astrophysics," Astrophys. J. **597**, 1266 (2003).
7. M. Gray, Jodrell Bank Centre for Astrophysics, School of Physics and Astronomy, University of Manchester, Oxford Road, Manchester M13 9PL, UK, is preparing a manuscript to be called "A photon orbital angular momentum model in an astrophysical maser."
8. B. Thidé, H. Then, J. Sjöholm, K. Palmer, J. Bergman, T.D. Carozzi, Ya. N. Istomin, N.H. Ibragimov, and R. Khamitova, "Utilization of Photon Orbital Angular Momentum in the Low-Frequency Radio Domain," Phys. Rev. Lett. **99**, 087701 (2007).
9. F. Tamburini, B. Thidé, G Molina-Terriza, and G. Anzolin, "Twisting of light around rotating black holes," Nature Phys. **7**, 195-7 (2011).

10. L. Allen, M. W. Beijersbergen, R. J. C. Spreeuw, and J. P. Woerdman, "Orbital angular momentum of light and the transformation of Laguerre-Gaussian laser modes," Phys. Rev. A. **45**, 8185-8189 (1992).
11. M.J. Padgett and L. Allen, "The Poynting vector in Laguerre-Gaussian laser modes," Optics Commun. **121**, 36 - 40 (1995).
12. A. V. Carpentier, H. Michinel and J. R. Salgueiro, "Making optical vortices with computer-generated holograms," Am. J. Phys. **76**, 916-921 (2008).
13. P. Schemmel, S. Maccalli, G. Pisano and B. Maffei, "Three dimensional measurements of a millimetre wave orbital angular momentum vortex," Opt. Lett. **39**, 626-629 (2014).
14. G.A. Turnbull, D.A. Robertson, G.M. Smith, L. Allen, and M.J. Padgett, "The generation of free-space Laguerre-Gaussian modes at millimetre-wave frequencies by use of a spiral phaseplate," Opt. Commun. **127**, 183-188 (1996).
15. M.W. Beijersbergen, R.P.C. Coerwinkel, M. Kristensen, J.P. Woerdman, "Helical-wavefront laser beams produced with a spiral phaseplate," Opt. Commun. **112**, 321-327 (1994).
16. M.V. Berry, "Optical vortices evolving from helicoidal integer and fractional phase steps," J. Opt. A: Pure Appl. Opt. **6**, 259-268 (2004).
17. D. Martin and J. Bowen, "Long-Wave Optics," IEEE Trans. Microw. Theory Tech. **41**, 1676-89 (1993).
18. P. Goldsmith, *Quasioptical Systems: Gaussian Beam Quasioptical Propagation and Applications ,* (IEEE Press, 1998).
19. J. D. Jackson, *Classical Electrodynamics Third Edition,* (John Wiley and Sons, Inc., 1998).
20. N. Trappe, J. A. Murphy and S. Withington, "The Gaussian beam mode analysis of classical phase aberrations in diffraction-limited optical systems," Eur. J. Phys. **24**, 403 - 412 (2003).
21. Y.S. Rumala and A.E. Leanhardt, "Multiple-beam interference in a spiral phase plate," J. Opt. Soc. Am. B. **30**, 615-621 (2013).
22. Y.S. Rumala, "Interference theory of multiple optical vortex states in spiral phase plate etalon: thick-plate and thin-plate approximation," J. Opt. Soc. Am. B. **31**, 615-621 (2013).
23. Y.S. Rumala, "Structured light interference due to multiple reflections in a spiral phase plate device and its propagation," Proc. SPIE **8999**, 899912 (2014).
24. R. L. Phillips and L. C. Andrews, "Spot size and divergence for Laguerre Gaussian beams of any order," Appl. Opt. **22**, 643 (1982).
25. V. Kotlyar and A. Kovalev, "Fraunhofer diffraction of the plane wave by a multilevel (quantised) spiral phase plate," Opt. Lett. **33**, 189-191 (2008).
26. P. Schemmel, S. Maccalli, B. Maffei, F. Ozturk, G. Pisano and M.W. Ng, "A Near Field 3D Scanner for Millimetre Wavelengths," in Proceedings of the 35th ESA Antenna Workshop on Antenna and Free Space RF Measurements, 10 - 13 September (2013), ESTEC, Noordwijk, The Netherlands.
27. F. Ozturk, B. Maffei and M. W. Ng, "A quasi-optical free-space s-parameters measurement system for material characterisation in W and Ka bands," in Proceedings of the 33rd ESA Antenna Workshop on Antenna and Free Space RF Measurements, 18 - 21 October (2011), ESTEC, Noordwijk, The Netherlands.
28. B. Maffei, S. Legg, M. Robinson, F. Ozturk, M. W. Ng, P. Schemmel and G. Pisano, "Implementation of a quasi-optical free-space s-parameter measurement system," in Proceedings of the 35th ESA Antenna Workshop on Antenna and Free Space RF Measurements, 10 - 13 September (2013), ESTEC, Noordwijk, The Netherlands.
29. P. Schemmel, Jodrell Bank Centre for Astrophysics, School of Physics and Astronomy, University of Manchester, Oxford Road, Manchester M13 9PL, UK, is preparing a manuscript to be called "Systematics Study of Spiral Phase Plate Designs for Millimetre Wave Orbital Angular Momentum State Manipulation."
30. M.S. Soskin, V. N. Gorshkov, M. V. Vasnetsov, J. T. Malos and N. R. Heckenberg, "Topological charge and angular momentum of light beams carrying optical vortices," Phys. Rev. A. **56**, 4064 (1997).

1. Introduction

Recently, there has been an increasing interest in the desire to use orbital angular momentum (OAM) states in communication systems [1]. Such systems promise high data transfer rates over a single frequency. Proof of concept experiments have shown such OAM based communication systems to be possible over optical [2, 3] and radio frequencies [4]. However, in order to become practical, these systems must handle a large number of OAM modes.

There is additional interest in trying to observe OAM modes from astrophysical sources [5–9]. Ideal astrophysical OAM observations would require the acquisition of an OAM mode spectrum, or a measure of the amount of power in each OAM mode emitted by a source. In order to accomplish this a telescope should be sensitive to multiple OAM modes.

In cylindrical coordinates, OAM beams are typically described by Laguerre Gaussian (LG) modes [10]. A single LG mode has the following form,

$$U_\rho^l(r,\phi,z) = A_\rho^l(r,z) L_\rho^{|l|}\left(\frac{2r^2}{w^2(z)}\right)\exp(il\phi)\exp\left[\left(\frac{ik_0 r^2 z}{2(z^2+z_R^2)}\right) - i(2\rho+|l|+1)\phi_0(z)\right] \quad (1)$$

where $A_\rho^l(r,z)$ is a complex amplitude, ρ is the radial mode number, l is the azimuthal mode number, $w(z)$ is the beam radius, k_0 is the free space wave number, z_r is the Rayleigh range, $\phi_0(z)$ is the Gaussian beam phase shift and $L_\rho^{|l|}(x)$ is the generalised Laguerre polynomial.

LG modes with a non-zero azimuthal mode number l contain phase discontinuities [Fig. 1(a)]. These discontinuities propagate outwardly from the centre of, and rotate around, the propagation axis. For this reason, LG modes with non-zero azimuthal mode numbers are said to contain a "phase vortex." The phase value at the "termination point," or origin of the dislocation, is undefined [Fig. 1(a)]. This undefined phase leads to a null in the intensity pattern [Fig. 1(b)], producing an annular ring shape [Fig. 1(c)].

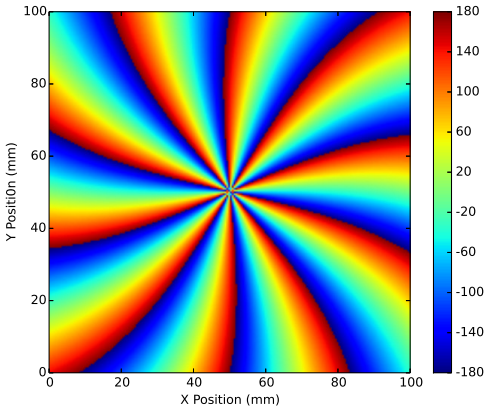

(a) Phase (Degrees)

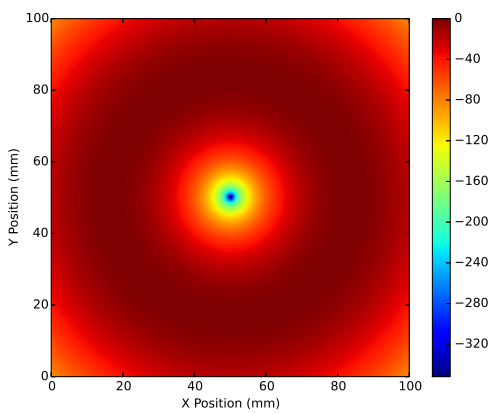

(b) Normalised Intensity (dB)

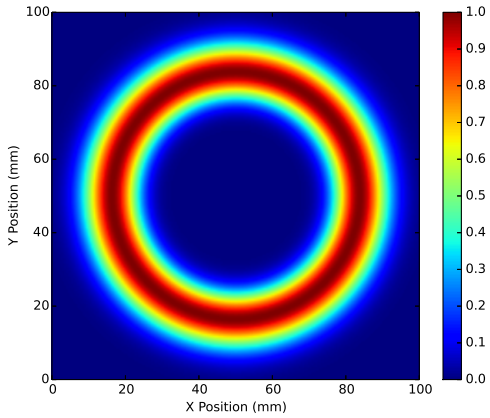

(c) Normalised Linear Intensity

Fig. 1: Expected phase (a), dB intensity (b) and linear intensity (b) patterns of a numerically generated LG beam with $l = 10$ and $\rho = 0$. The central intensity null is caused by the undefined phase at the end of each phase dislocation. Each dislocation is curved because the LG mode was plotted away from the beam waist.

For a beam with $\rho = 0$ the radius of maximum intensity is [11],

$$r_{max} = w(z)\sqrt{\frac{l}{2}} \tag{2}$$

In optical systems, large numbers of OAM modes are typically manipulated with a diffractive hologram [12] displayed on spatial light modulator, but similar systems do not exist for millimetre and radio frequencies due to the relatively large wavelengths.

The simplest device to manipulate OAM modes at millimetre frequencies is a spiral phase plate (SPP) [13–15]. A SPP is a dielectric slab of material with an azimuthally dependent thickness that imparts an azimuthal phase shift onto incident radiation (Fig. 2). The total step height, h of the SPP is chosen so that the total phase shift around the centre of the SPP is an integer multiple of $2\pi l$, where l is an integer. This imparts a change to the incident radiation's azimuthal mode number l, such that,

$$\Delta l = \frac{h\Delta n}{\lambda} \tag{3}$$

where Δn is the change in the refractive index between the dielectric material and the surrounding medium, and λ is the incident wavelength.

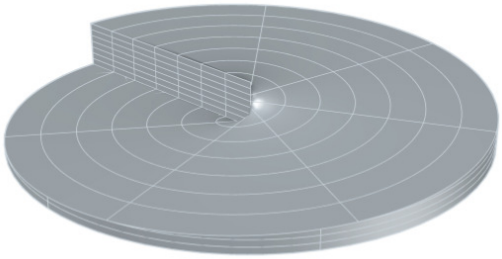

Fig. 2: A CAD model of a smooth surfaced $\Delta l = \pm 1$ SPP.

One can envision that future millimetre and radio OAM sensitive systems will manipulate the large number of modes required by using several interchangeable SPPs with $\Delta l = \pm 1, \pm 2, \ldots \pm N$ where N is some integer. There are two standard approaches to manufacture SPPs with $|\Delta l| > 1$. The first is to simply increase the step height h. The second approach is to compress the behaviour of an $l = 1$ SPP into a specified angular region, a "split," configuration. To accomplish this, a certain number of $\Delta l = \pm 1$ SPPs (specifically a number $b = |l|$) can be restricted to angular regions of $\theta_b = 2\pi/b$. Additionally, the smooth SPP surface may be approximated by a series of discrete steps. Figure 3 shows a $\Delta l = \pm 2$ ($\theta_b = \pi$) SPP model with a stepped surface in a split configuration.

Dielectric SPPs are typically machined from a single piece of material. Although this is a simple process, accuracy near the centre region of the plate has to be compromised due to the finite size of the milling tools. This leaves some sections of the SPP cut to an improper height. This results in fractional step heights and the subsequent generation of a non-integer Δl Eq. (3). Fractional step heights force the creation and annihilation of additional vortices [16], resulting in a beam with an undesired mode content.

A solution to the problem is to machine each SPP section, or module, individually and assemble them into the full plate afterwards. Doing so allows each section to be machined to the proper height, limiting mode contamination. To test this concept a modular split stepped

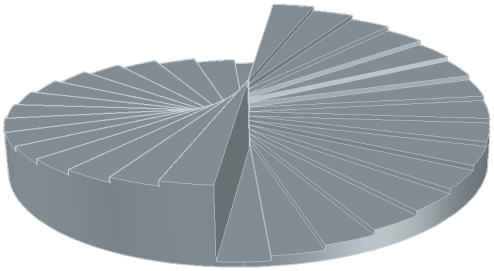

Fig. 3: A CAD model of a "split stepped," SPP. Here two $\Delta l = \pm 1$ SPPs were compressed from an angular range of $[0, 2\pi]$ to $[0, \pi]$ and pushed together in order to generate an $l = \pm 2$ LG beam.

$\Delta l = \pm 10$ SPP was designed and manufactured [Fig. 4(a)] from polypropylene ($n \approx 1.50$) for use at 100 GHz ($\lambda = 3$ mm).

The full spiral is comprised of ten individual modules [Fig. 4(b)], which have machined steps on the top and bottom to minimise the height change between the largest and smallest steps. Each module has an additional tongue and groove on the surfaces parallel to the beam propagation. These are used to attach each module together and to insure proper alignment between them.

(a) Full $\Delta l = \pm 10$ SPP

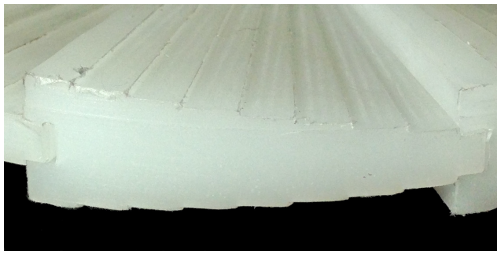

(b) A single module of the full SPP

Fig. 4: A full $\Delta l = \pm 10$ SPP (a). A single module from the full SPP showing the tongue and groove interlocking system (b).

2. Gaussian beam mode analysis

In general, SPPs are not pure mode converters, but instead produce a superposition of LG modes [15]. Multiplying a pure LG mode by $exp(-i\Delta l\phi)$ alters the incident mode number l so that the transmitted beam has an azimuthal phase term $exp(-il'\phi)$, where $l' = l_{in} + \Delta l$. However, the azimuthal mode numbers in the complex amplitude $A_p^l(r,z)$ remain unchanged. Therefore, the complex amplitude term utilises l_{in}, while the azimuthal phase shift term contains l'. This results in an impure LG mode, which must be described as a superposition of pure LG modes. It should be noted that while a perfectly manufactured SPP with antireflection coatings will produce perfect LG beams with respect to the azimuthal mode number, a superposition of radial modes will always exist. The modal description of SPPs may be found by using Gaussian Beam

Mode Analysis (GBMA) [17, 18], when the input beam divergence and SPP step height h, are small [15]. In GBMA, any arbitrary square integrable function on the interval (a,b) can be described by a superposition of orthonormal functions [19].

$$U_m^n(r,\phi,z) = \sum_{l=-\infty}^{\infty} \sum_{\rho=0}^{\infty} a_{\rho,m}^{l,n} U_\rho^l(r,\phi,z) \tag{4}$$

where, U_ρ^l are the LG modes if a cylindrical coordinate system is adopted. The mode coefficients $a_{\rho,m}^{l,n}$ are found by [15],

$$a_{\rho,m}^{l,n} = \left\langle U_\rho^l | U_m^n \right\rangle \tag{5}$$

Here the brackets denote an integration on the plane perpendicular to the propagation axis z (this is the (r,ϕ) plane in cylindrical coordinates). An arbitrary phase shift may be introduced into the system by multiplying the input field by $exp(-i\Phi)$ [20]. For SPPs, the function Φ is required to induce an azimuthal phase shift of Δl, found using Eq. (3). Therefore, the phase shift term for a SPP is $exp(-i\Delta l\phi)$ [15]. Introducing the phase shift term to Eq. (4) gives,

$$U_m^n(r,\phi,z) = \sum_{l=-\infty}^{\infty} \sum_{\rho=0}^{\infty} a_{\rho,m}^{l,n} U_\rho^l(r,\phi,z)\, exp(-i\Delta l\phi) \tag{6}$$

which then implies that,

$$a_{\rho,m}^{l,n} = \left\langle U_\rho^l\, |exp(-i\Delta l\phi)|\, U_m^n \right\rangle \tag{7}$$

Finally, the mode spectrum, or fraction of power of the input field U_ρ^l contained in each mode U_m^n is found by calculating the normalised coupling coefficient for each mode.

$$\left| C_{\rho,m}^{l,n} \right|^2 = \frac{\left| \left\langle U_\rho^l\, |exp(-i\Delta l\phi)|\, U_m^n \right\rangle \right|^2}{|\langle U_m^n | U_m^n \rangle|^2} \tag{8}$$

3. Numerical simulations

Mode spectra [Eq. (8)] for various SPP designs may be calculated numerically. Additionally, the phase shift function Φ, which is normally smooth and continuos, may be discretised to mimic stepped SPP designs. Machining tolerances may also be accounted for by allowing each SPP step to vary from the designed thickness by some small random amount. It should be noted that multiple reflections are a significant effect and are not taken into account by the model in Sec. 2 [21–23]. In addition, other factors could also be taken into consideration, such as machining errors as a function of radius, the effects of transmission through the dielectric, inhomogeneities of the index of refraction or the finite size of the SPP.

To compare the effect of a stepped to a smooth SPP, numerical simulations of a $\Delta l = 1$ SPP illuminated with a U_0^0 Gaussian beam were conducted on a field eight times the input beam width (to ensure proper convergence) on a grid of 200×200 points. The stepped SPP was comprised of sixteen steps without random variations in thickness. The decomposition results (Table 1) for both the smooth and stepped SPP show that all of the initial Gaussian power was converted into a LG beam with $l = 1$. However, since the SPP is not a pure mode converter, radial modes with $\rho \neq 0$ are also present. It should also be noted that the mode content for each (l,ρ) pair generated by the sixteen stepped SPP is lower than for the smooth SPP. This is a result of leakage from modes containing a large fraction of the incident power, to modes containing

less power. Analysis of each mode in Table 1 shows that there is roughly a 2.7 percent drop in power in the first six modes.

Table 1: Mode content, in percentages, of a U_0^0 beam passed through a smooth and a sixteen stepped $\Delta l = 1$ SPP.

Smooth	$l = 1$	78.56	9.82	3.68	1.92	1.18	0.79
Stepped	$l = 1$	76.35	9.54	3.58	1.86	1.14	0.77
	$\rho =$	0	1	2	3	4	5

These numerical simulations can be repeated for the modular $\Delta l = \pm 10$ SPP. Table 2 shows the first eight radial modes of the decomposition of a smooth and an eight-steps-per-mode split configuration $\Delta l = 10$ SPP. Immediately obvious are the extremely low mode contents.

Table 2: Mode content, in percentages, of a U_0^0 beam passed through a smooth and an eight-steps-per-mode $\Delta l = 10$ SPP.

Smooth	$l = 10$	0.40	0.90	1.35	1.70	1.94	2.10	2.19	2.22
Stepped	$l = 10$	0.35	0.80	1.20	1.51	1.73	1.87	1.95	1.99
	$\rho =$	0	1	2	3	4	5	6	7

This is due to a mismatch between the generated beam's and decomposition mode's azimuthal mode numbers in the complex amplitude term $A_\rho^l(r,z)$ and azimuthal phase term $exp(-il'\phi)$. While the decomposition modes use the same azimuthal mode number in both the complex amplitude and azimuthal phase term, the generated beam does not. Here, the complex amplitude utilises an azimuthal mode number of $l_{in} = 0$, yet the azimuthal phase term uses $l' = \Delta l$. Since the spot size of an LG mode is dependent on both ρ and l [24], the generated beam will have a smaller radius then the decomposition modes. Therefore, a higher number of radial modes must be included in the decomposition in order to describe the generated beam. Alternatively, the beam waist of the decomposition modes may be optimised in order to concentrate the mode spectra into a primary mode [18, 20]. This has the advantage of reducing the number of modes needed to describe the generated beam, thereby speeding up computation time. Several mode spectra were calculated to determine the optimal decomposition beam waist. Figure 5 shows the maximum mode coefficient as a function the decomposition beam waist. The mode content is maximised in a primary mode when the decomposition beam waist is 7.5 mm. Optimised mode spectra for a smooth and split stepped configurations are shown in Table 3.

Table 3: Mode content, in percentages, of a U_0^0 beam passed through a smooth and an eight-steps-per-mode $\Delta l = 10$ SPP, with an optimised decomposition mode beamwaist of 7.5 mm.

Smooth	$l = 10$	52.01	0.00	16.61	0.04	8.14	0.13	4.56	0.21
Stepped	$l = 10$	45.38	1.40	15.09	1.71	7.27	1.71	4.31	1.45
	$\rho =$	0	1	2	3	4	5	6	7

Now that the mode coefficients for the modular $\Delta l = \pm 10$ SPP are known, Eq. (4) may be used to propagate and reconstruct the final field as a mode superposition. Using a wavelength of $\lambda = 3$ mm, a beam waist, $\omega_0 = 25$ mm (this is representative of the beam waist used in the experimental setup. See Sec. 4) and a propagation distance of 40λ (120 mm) and 73.3λ (220 mm) respectively, the expected beam intensity and phase may be plotted (Fig. 6). These

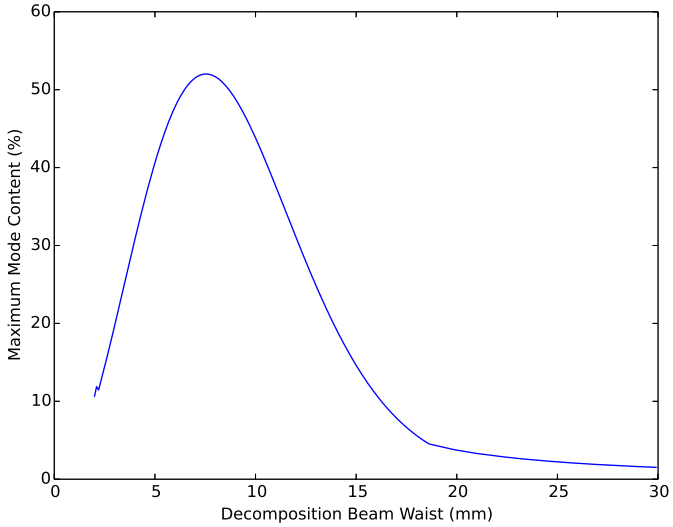

Fig. 5: Maximum mode content as a function of the decomposition beam waist has a maximum of 52.01% at 7.5 mm.

simulations were done on a grid 100 mm $\times$ 100 mm with a resolution of 0.5 mm in either direction and decomposed over the modes $-40 \leq l \leq 40$ and $0 \leq \rho \leq 40$ in order to ensure proper convergence.

Both intensity simulations [Fig. 6(a) and Fig. 6(c)] show a pattern comprised of a semi-discrete ring with a shallow inner intensity island surrounded by a deep intensity trough. Ten intensity peaks make up the semi-discrete ring, which is a result of the ten singular modules of the SPP model. Phase calculations on the 40λ (120 mm) surface [Fig. 6(b)] show ten primary dislocation lines broken by a radial node, leaving ten smaller dislocations inside the radial break. A further break in the dislocation lines is visible in the 73.3λ (220 mm) phase pattern [Fig. 6(d)]. Note that the dislocation lines do not meet in the centre of the propagation axis, as is the case for the pure $l = 10$ LG mode in Fig. 1(a). This is due to the increase of non-zero radial modes in the mode spectrum generated by the SPP.

Although the GBMA model presented did not take into account thickness dependent reflection losses in a dielectric slab, such effects are known to be pronounced in typical dielectric etalons. Therefore, losses for each step height (Table 5) of the modular SPP were calculated using a simple transmission line code (Fig. 7). Maximum transmission was near 100% while the minimum transmission was 85.2%. Specifically, the simple transmission line code predicted a minimum transmission of 85.2071%, which may be compared to the multiple reflections, thin plate approximation [21] predicted value of 85.2074%. It is clear that transmission modulation due to multiple reflections inside the dielectric is a small effect. However, multiple reflections in a dielectric SPP also introduce unwanted azimuthal modes, which may lead to azimuthal modulations in intensity [21–23]. Furthermore, standing waves inside the dielectric may also affect transmission. For example, the second and sixth largest step heights are on average 3.04λ and 1.95λ tall. Since these steps are nearly integer multiples of the incident wavelength standing waves could be produced.

Finally, it is known that discretising a SPP with too few steps will induce azimuthal intensity modulations [25]. Therefore, the RMS error between the intensity patterns of a perfectly smooth $\Delta l = \pm 10$ SPP and modular split stepped $\Delta l = \pm 10$ SPP, as a function of the number of total

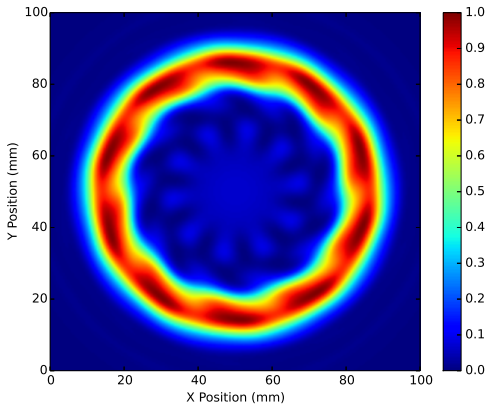

(a) Normalised intensity on the 40λ (120 mm) surface.

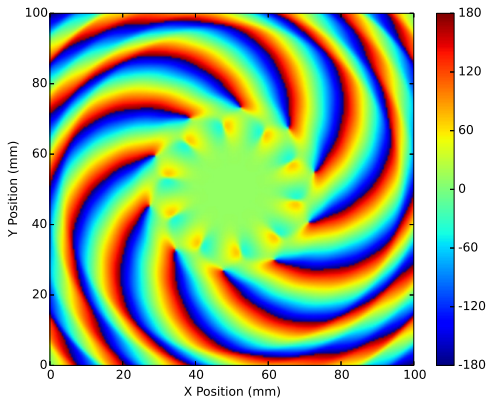

(b) Phase (Degrees) on the 40λ (120 mm) surface.

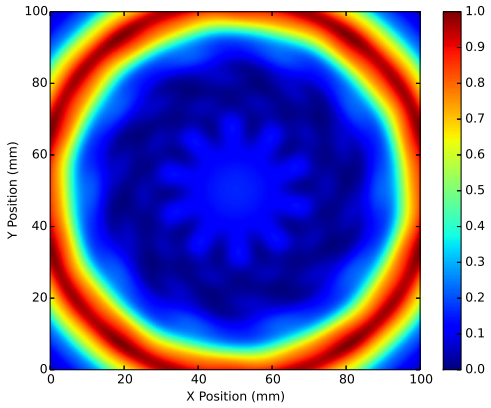

(c) Normalised intensity on the 73.3λ (220 mm) surface.

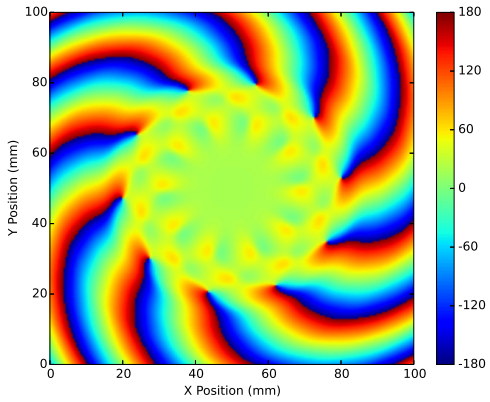

(d) Phase (Degrees) on the 73.3λ (220 mm) surface.

Fig. 6: Numerical simulations of a $\Delta l = 10$ stepped SPP in a split configuration. The normalised linear intensity on both the 40λ (120 mm) [Fig. 6(a)] and 73.3λ (220 mm) [Fig. 6(c)] measurement surfaces display a discontinuous intensity ring when compared with Fig. 1(c). The calculated phase on both surfaces also differs from the pure $(l = 10, \rho = 0)$ pattern [Fig. 1(a)]. In both Fig. 6(b) and Fig. 6(d) radial modes generate discontinuities in the phase dislocation lines.

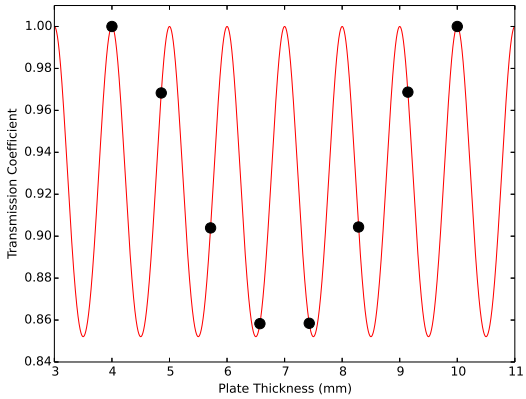

Fig. 7: Transmission coefficients calculated as a function of SPP thickness (red line). Black dots indicate the eight individual step heights that make up the modular SPP.

steps was calculated (Table 4). Using eight-steps-per-mode, or a total of eighty steps, results in a 1.37% RMS error in the intensity pattern. Following the criteria set out in [25] where an RMS error of less then 2% is acceptable, a polypropylene $\Delta l = \pm 10$ modular split stepped SPP for use at 100 GHz should have at least seven-steps-per-mode.

Table 4: RMS intensity pattern error as a function of the number of steps per mode between a perfect and modular split stepped $\Delta l = \pm 10$ SPP.

Steps per mode	RMS (%)
4	12.02
5	5.01
6	2.93
7	1.98
8	1.37
9	1.01
10	0.80

4. Measurement system and SPP parameters

A three dimensional W-band ($75 - 100$ GHz) scanning system was used to record the data [13, 26]. The scanner has a 50 cm $\times$ 50 cm $\times$ 50 cm working volume, and uses a WR-10 rectangular to circular waveguide transition with a 3.0 mm opening diameter as a field probe. To minimise reflections between the probe and SPP, a 3D printed pyramidal absorber was placed around the probe opening. The modular SPP was illuminated with a quasi-planar Gaussian beam created with a compact test range antenna (CTRA) [Fig. 8(a)] designed for material characterisation [27, 28]. The CTRA section is comprised of a source antenna, sub reflector and main reflector, which generates a Gaussian beam [Fig. 8(b)] profile with planar phase fronts [Fig. 8(c)] approximately 265 mm from the main reflector. A horizontal cut was taken through the centre of the beam with a positioning resolution of 0.5 mm and utilised five measurement sweeps.

The SPP was placed in a custom designed mount and centred on the CTRA beam. The surrounding area was covered with radiation absorbing material. Measurements across three

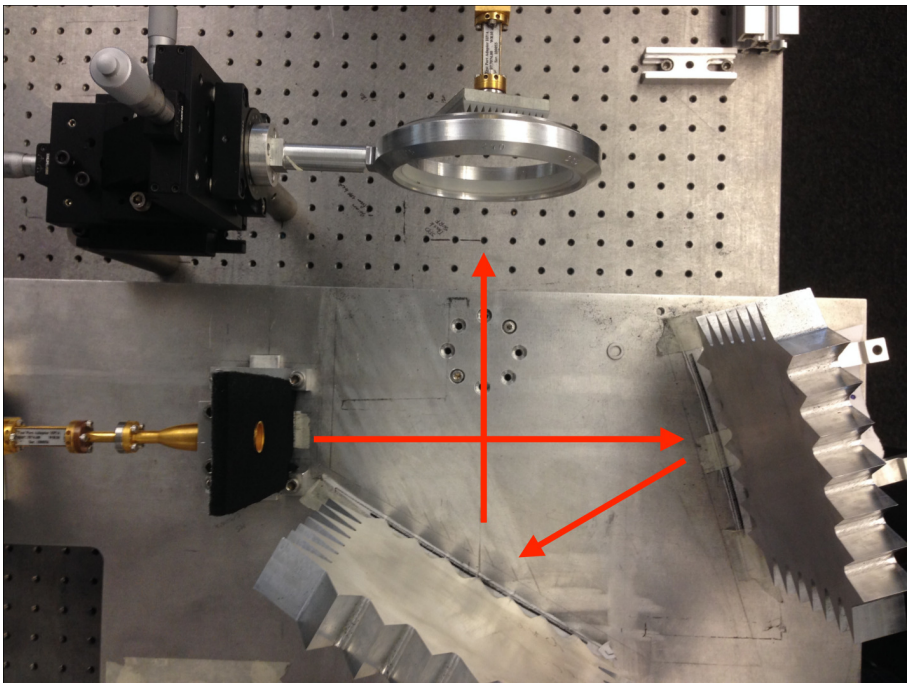

(a) Incident beam optical path.

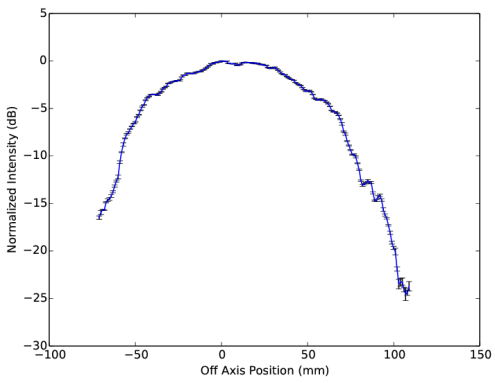

(b) Incident Intensity (dB)

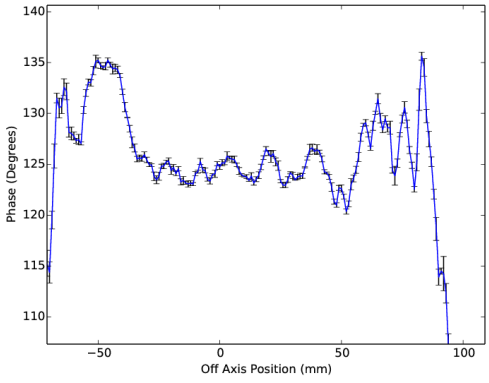

(c) Incident Phase (Degrees)

Fig. 8: A Gaussian beam is generated by the feed horn and is reflected by both CTRA mirrors. The beam then propagates to the SPP mount and is measured by the WR-10 probe [Fig. 8(a)]. (Not pictured is the absorbing material surrounding the mounting structure.) The measured incident Gaussian beam created by the CTRA source with vertical error bars denoting one standard deviation of the five measurement sweeps [Fig. 8(b)]. Measured near planar phase front at the beam waist created by the CTRA source with vertical error bars denoting one standard deviation of the five measurement sweeps [Fig. 8(c)].

surfaces perpendicular to the propagation axis were carried out at distances of 6.7λ, 40λ and 73.3λ (20 mm, 120 mm and 220 mm, Figs. 9 - 11) behind the modular SPP. As the far field of this system is greater then one metre, each surface cut is well within the near field of the SPP. Each surface cut was centred on the propagation axis, comprising of a $33.3\lambda \times 33.3\lambda$ (100 mm $\times$ 100 mm) scan area, while the probe had a mechanical positioning resolution of 0.17λ (0.5 mm) in both directions. Due to the presence of phase fluctuations [Fig. 8(c)] in combination with diffraction effects generated by the SPP mount, background measurements were taken without the modular SPP and were used to correct the SPP measurements. Background phase data was subtracted from the SPP generated phase in order to produce normalised phase patterns. The incident beam waist was 41 mm while the averaged edge taper at the SPP mount inner edge was -4.77 dB. Additionally, measured background intensity on each plane (not presented here) did not indicate any azimuthal intensity modulations.

Table 5 shows the measured average height and standard deviation for each SPP step. Additionally, the measured average difference from the expected $\Delta h = 6.00$ mm primary step height was 0.07λ with a standard deviation of 0.06λ.

Table 5: Measured average and standard deviation step heights for the manufactured $\Delta l = \pm 10$ modular split stepped SPP.

Step Number	1	2	3	4	5	6	7	8
Average Height (mm)	9.88	9.13	8.26	7.45	6.63	5.85	4.99	4.10
Standard Deviation (mm)	0.12	0.14	0.23	0.21	0.21	0.21	0.20	0.22

5. Results

Measured normalised intensity and phase results on the 6.7λ (20 mm) surface cuts are presented in Fig. 9(a) and Fig. 9(b) respectively. Due to the close proximity of the probe to the plate, the intensity pattern is dominated by the varying transmission (Fig. 7) of the incident beam through the individual SPP steps. Each of the ten modules, or sections, are visibly separated by a pair of radial lines of high intensity. Each radial line of high intensity corresponds to the thickest and thinnest section of the SPP, respectively. A small line of lower intensity separates the two high intensity lines and is the result of a boundary condition mismatch between the field inside and outside the largest modular SPP step. It is clear from the intensity data (Fig. 9) that variations larger than the $\approx 15\%$ predicted by simple transmission line or multiple reflection codes (Sec. 3) exist. This is currently under study [29]. Therefore, we must conclude that there is some other effect creating the observed larger variations. Background normalised phase in Fig. 9(b) indicates that the modular SPP functioned properly, and generated the desired $\Delta l = \pm 10$ change in mode number. Ten dislocation lines are clearly visible, radiating outwards, from the centre of the beam. Each dislocation line abruptly ends at a "termination point," resulting in a "phase vortex." The exact value of the phase at the termination point is undefined, resulting in an intensity null. Additionally, the phase circulates by an amount of 2π around each termination point. The integrated phase shift around the beam is $2\pi l$, in this case 20π.

Normalised linear intensity of the 40λ (120 mm) surface is presented in Fig. 10(a). The intensity ring expected in beams with a non-zero azimuthal mode number is clearly visible. However, it is not continuous, but is instead broken into ten pairs of high intensity regions.

Transmission through each SPP step alone can not entirely account for the intensity pattern produced. Diffraction from the largest SPP steps introduces discontinuities between each pair of high intensity peaks. In addition, individual steps form a triangular aperture, which introduces additional diffractive effects. A study comparing several SPP configurations, utilising different

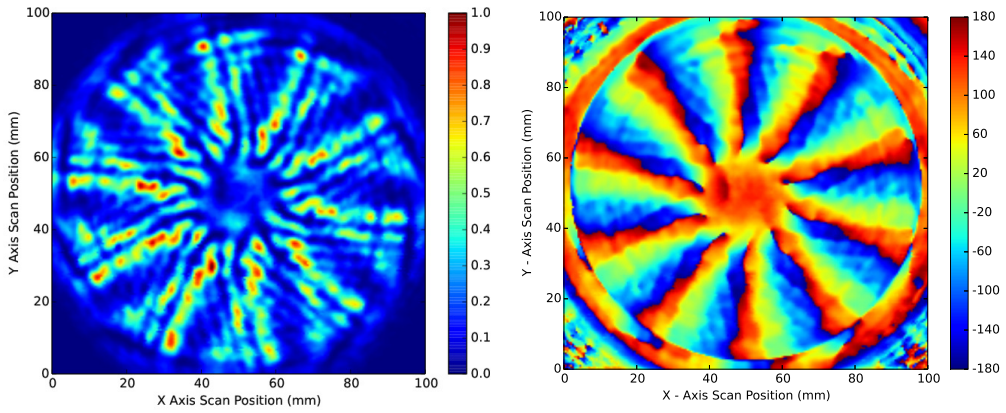

(a) Normalised Intensity

(b) Background Normalised Phase

Fig. 9: Measured 6.7λ (20 mm) surface normalised intensity pattern (Units in (V/m)) [Fig.9(a)] shows a near field "image," of the modular SPP is a result of the variable transmission through the SPP dielectric. Background normalised phase data (Units in degrees) for the 6.7λ (20 mm) surface [Fig.9(b)] contains ten phase dislocations, indicating that the modular SPP imparts a change in mode number of $\Delta l = \pm 10$.

source configurations, and finite element analysis modelling is being conducted to further understand how these additional effects interact to produce the generated SPP beams [29]. Intensity peak splitting could either be due to the added surface boundaries between the tongue and groove regions, or further machining imperfections. This splitting could be lessened, or perhaps removed entirely, with improvements to the interfacing between the modules while the continuity of the intensity ring could be improved by using more steps-per-mode.

Figure 10(b) shows the phase results for the 40λ (120 mm) surface. Ten phase dislocations are visible at a radial distance of approximately 30 mm from the centre of the beam. Inside this radial distance the phase is distorted. Recalling the phase results in Fig. 6, the first ring of broken dislocations may be attributed to the increase of radial mode strength resulting from the discrete SPP surface. Additional inner dislocation pairs are produced by complex interference between each step of an individual module. The interference becomes more pronounced as the width of each step decreases. This effect in combination with machining imperfections produce a beam with a fractional mode number [16].

Intensity and phase results for the 73.3λ (220 mm) surface are presented in Fig. 11. Still visible is the primary intensity ring, which has diverged as expected according to Gaussian beam propagation [18]. The central intensity peak is still visible in Fig. 11(a).

More interesting is the phase pattern. Whereas the phase in the centre of Fig. 10 was distorted and included additional dislocations, the phase in Fig. 11(b) is smoother. There are still ten outer dislocation lines, indicating that the beam has an azimuthal mode number of $l = 10$. Eight of the outer phase dislocations are also associated with a smaller dislocation pair at a small radii. These are due to radial modes generated by the SPP breaking the phase dislocation lines. However, the additional dislocations in the centre of Fig. 10(b) have largely disappeared. This appears to be evidence of the annihilation of phase vortices as described by [16]. The annihilation of phase vortices is not unexpected, and has been discussed in theory and experiments of the free-space propagation of light waves [30].

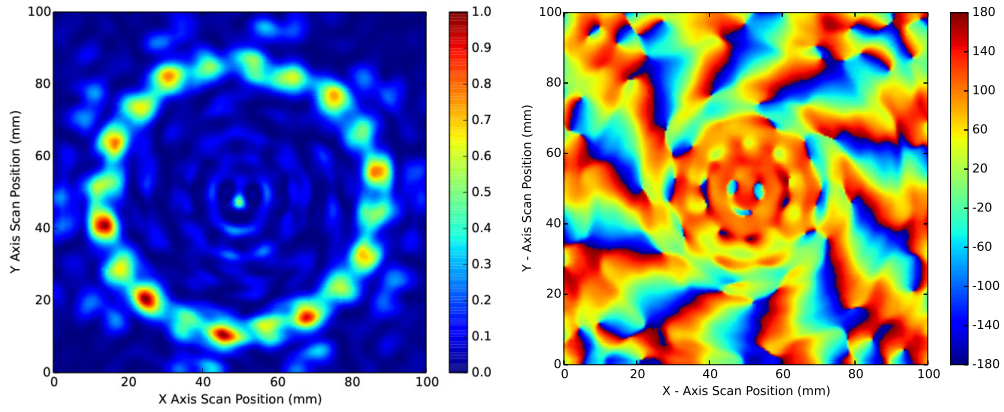

(a) Normalised Intensity

(b) Background Normalised Phase

Fig. 10: Normalised linear intensity pattern (Units in V/m) for the 40λ (120 mm) surface [Fig. 10(a)]. The expected intensity ring has developed and is clearly visible, although it remains discontinuous. Phase (Units in degrees) measured on the 40λ (120 mm) surface [Fig. 10(b)] shows ten outer phase dislocations and a largely distorted centre. Phase distortions in the centre of the pattern are produced by complex interference as the width of each SPP step decreases with a decreasing radius and machining imperfections.

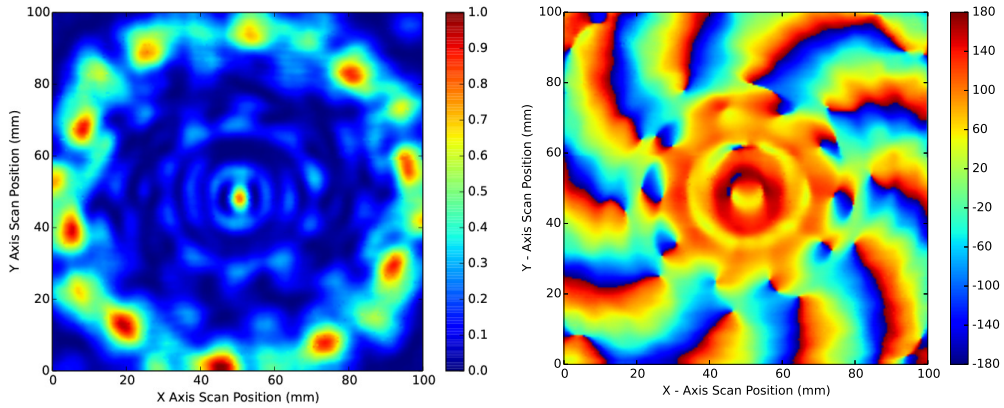

(a) Normalised Intensity

(b) Background Normalised Phase

Fig. 11: Measured normalised linear intensity (Units in V/m) of the 73.3λ (220 mm) surface [Fig. 11(a)], showing the OAM intensity ring resulting from the undefined phase at the termination point of the dislocation lines. Background normalised phase (Units in degrees) on the 73.3λ (220 mm) surface [Fig. 11(b)] contains ten outer phase dislocations at radial distances greater then 30 mm. The clean central region, especially compared to that in Fig. 10, indicates the possible annihilation of phase vortices.

6. Conclusions

There is a growing interest in manipulating OAM modes for use in millimetre and radio wave communication and astronomical observing systems. One of the simplest ways to manipulate OAM modes is through the use of a SPP. Using several interchangeable SPPs, one for each specific mode, may be one way to handle a large set of OAM modes with future radio communication and astronomy systems. Manufacturing SPPs for large mode numbers becomes difficult using standard techniques. To alleviate this problem, a proof of concept, modular stepped SPP was design, manufactured and tested at 100 GHz. The modular SPP consists of ten separate sections that interlock to create the full $\Delta l = \pm 10$ plate assembly. The near field intensity and phase of the full SPP was measured in 100 mm $\times$ 100 mm surface cuts perpendicular to the propagation axis at 6.7λ, 40λ and 73.3λ (20 mm, 120 mm and 220 mm) from the SPP. Phase results showed that the modular SPP induced an azimuthal mode number change of $\Delta l = \pm 10$. The 40λ (120 mm) and 73.3λ (220 mm) intensity patterns indicated that the modular interlocking method and stepped surface were causing some discontinuities in the expected intensity ring pattern. These systematics can be improved with modified plate designs. However, the modular SPP concept was proven to function properly.

Phase results did show some additional interesting properties. Initial and final near field surfaces showed that there were ten phase dislocations indicating a $|l| = 10$ beam. Yet, the 40λ (120 mm) surface showed that the phase at the centre of the beam was largely distorted. The large number of extra dislocations seem to point at the creation and annihilation of phase vortices. These effect are currently under study using other plate designs and incident source beam configurations in order to isolate them in future analysis.

Acknowledgments

The authors would like to thank Mr. Saul Beeson for his outstanding dedication and craftsmanship in creating the modular SPP used for this paper. The authors also acknowledge support from the Science Technology Facilities Council (STFC).